


Article

Strength Characteristics and Micro-Mechanism of Silty Soil Modified by Red Mud Co-Cement

Xinming Li ¹, Pan Yan ¹, Song Yin ^{1,*}, Xianwei Zhang ², Pengfei Liu ¹ and Yulong Wang ¹

¹ School of Civil Engineering and Architecture, Zhongyuan University of Technology, Zhengzhou 450007, China; xml@zut.edu.cn (X.L.)

² State Key Laboratory of Geomechanics and Geotechnical Engineering, Institute of Rock and Soil Mechanics, Chinese Academy of Sciences, Wuhan 430071, China

* Correspondence: syin@zut.edu.cn

Abstract: Red mud (RM) is a kind of solid waste produced during the bauxite refining process, which can cause significant environmental pollution when stored in large quantities. To address this issue and to improve the reuse rate of RM, this study investigates the feasibility of using RM as a roadbed filling material, specifically in combination with cement, using modified silty sand (P.O-RMS). Therefore, mechanical and microscopic tests are conducted with different RM contents (W_{RM}), cement contents ($W_{P.O}$), and curing ages to analyze the P.O-RMS' strength, deformation characteristics, and microstructure formation mechanism. Additionally, the radioactivity and heavy metal concentrations of P.O-RMS are also detected. Mechanical test results showed that the unconfined compressive strength (UCS) of P.O-RMS does not increase monotonically with the increase of W_{RM} , and the peak strength appears at $W_{RM} = 20\%$. Although adding RM has a negative impact on the toughness of P.O-RMS at the initial curing ages of 7 days and 28 days, they still meet the requirements of the Chinese standard for high-grade highway base strength. Scanning electron microscope testing shows that the gel products produced by cement hydration increase with the amount of RM, and reach their maximum at $W_{RM} = 20\%$. Therefore, $W_{RM} = 20\%$ is recommended as the optimum admixture of P.O-RMS. The usage of RM as a filling material for roadbed construction in this study not only aligns with the principles of sustainable development, but also provides a crucial theoretical foundation for the effective utilization of RM resources.

Keywords: red mud; cement; silty soil; unconfined compressive strength; micro-mechanism



Citation: Li, X.; Yan, P.; Yin, S.; Zhang, X.; Liu, P.; Wang, Y. Strength Characteristics and Micro-Mechanism of Silty Soil Modified by Red Mud Co-Cement. *Sustainability* **2023**, *15*, 8762. <https://doi.org/10.3390/su15118762>

Academic Editor: Castorina Silva Vieira

Received: 20 March 2023

Revised: 7 May 2023

Accepted: 10 May 2023

Published: 29 May 2023



Copyright: © 2023 by the authors. Licensee MDPI, Basel, Switzerland. This article is an open access article distributed under the terms and conditions of the Creative Commons Attribution (CC BY) license (<https://creativecommons.org/licenses/by/4.0/>).

1. Introduction

Red mud (RM), a by-product of the bauxite smelting process, is increasing in quantity as the global demand for aluminum continues to grow. As estimated, the world capacity for RM production is 160 million tons per year, with China accounting for 70 million tons [1]. However, the comprehensive utilization rate of RM remains low. Currently, the treatment of RM in China is mainly in storage [2], which consumes vast areas of land and causes dust pollution after dehydration and weathering. RM is a material with high alkaline, heavy metal elements, and radioactivity, causing intense alkaline erosion of surrounding buildings and soil, seepage of radioactive and toxic substances into groundwater, and water contamination [3]. Therefore, the large-scale utilization of RM needs to be solved urgently.

According to previous research, RM has been applied for metal extraction [4,5], preparation of adsorption materials [6,7], and road-building material. Among these methods, the most efficient way to consume a large amount of RM is to produce building materials. RM contains a lot of renewable active substances, such as aluminum, silicon, and calcium, which are the main reason for its use as a road-building material. Based on alkali excitation, RM can combine with other auxiliary materials to generate high-strength cementitious materials [8]. Recently, many researchers have paid more attention to the

feasibility and effectiveness of RM as a road-building material, and some progress has been made. Garanayak et al., 2021, found that the strength of cementitious materials mixed from different proportions of cement and RM varied with their mixture ratio and curing environment, and found that ettringite and amorphous CSH gels are the main factors of strength variation [9]. Yang et al., 2020, blended cement, lime, and slag into comprehensive modified materials according to 8% of RM dry weight, reducing RM's limiting water content and improving the overall strength and water stability [10]. In addition, Sun et al., 2018, utilized composite materials such as cement to modify the RM. The results indicated that all indices of the RM are substantially improved, the unconfined compressive strength (UCS) of the modified material in 3 d is greater than 3.0 MPa, and the road properties all meet the relevant application standards [11]. Ma, Q et al., 2022, demonstrated the feasibility of using RM as road base stabilization material. They found that the addition of 30–42% RM can effectively improve the lateral limitless compressive strength of loess. Moreover, RM can promote the production of hydration products and improve the compactness of the structure [12]. Ma, S et al., 2022, modified RM with cement, phosphogypsum, and organic polymers and evaluated the performance of the P.O-RMS as a road base. It was found to have less than 20% loss of strength when immersed in water for 7 and 28 days, and has good bearing capacity as a road base [13]. After reviewing the literature, it has been found that Recycled Materials (RM) can meet the necessary mechanical properties required for road materials. However, there is a limited amount of research regarding the use of RM as an inorganic binder to stabilize pavement subgrade material. Furthermore, there is a major gap in understanding the strength formation mechanisms of RM and its environmental impact. Therefore, the environmentally friendly utilization of RM in road engineering needs further study.

This paper aims to explore the feasibility of RM and cement-modified silty sand (P.O-RMS) for roadbed construction, as well as to determine the optimal proportion for achieving better mechanical properties. Therefore, UCS tests are conducted on P.O-RMS specimens with different RM contents (W_{RM}), cement contents (W_{PO}), and curing ages to obtain the optimal proportion of RM and cement. Moreover, the hydration products and microstructures of the RM co-cement modified silty soil (P.O-RMS) are analyzed by scanning electron microscopy (SEM), X-ray diffraction (XRD), and thermogravimetric-differential thermal analysis (TG-DTG) microscopy tests. This work provides a theoretical basis and technical support for the reuse of red mud, sustainable development, and environmental improvement. The technical route of this paper is shown in Figure 1.

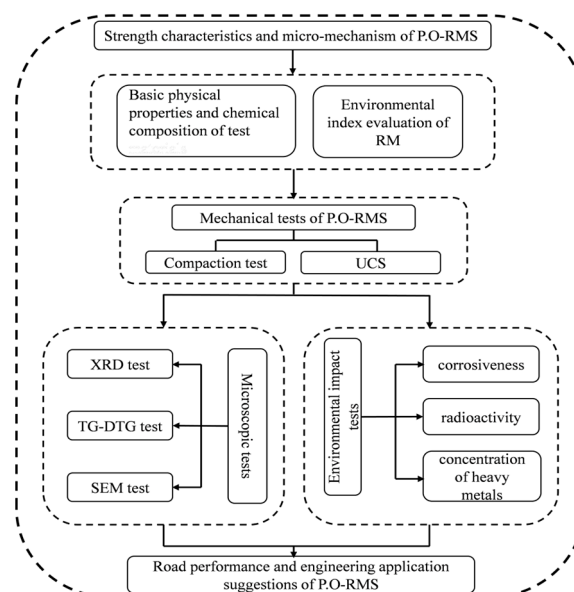


Figure 1. Technical route flow chart.

2. Materials and Methods

2.1. Materials

The silty soil used in this study was obtained from Zhengzhou City, Henan Province, China. Furthermore, the RM was obtained from the alumina production using the Bayer process in a bauxite plant in Henan Province. The physical properties of the soil and the RM (see Table 1). It can be seen from Table 1 that RM has high liquid plasticity limit and strong hydrophilicity.

Table 1. Basic physical properties of the selected materials.

| Physical Property | Materials | |
|---|------------|--------------|
| | Silty Soil | Red Mud (RM) |
| Specific gravity | 2.65 | 2.83 |
| Plastic limit (%) | 8.2 | 33.8 |
| Liquid limit (%) | 19.2 | 50.2 |
| Plasticity index | 11 | 10.4 |
| Optimum water content (%) | 9.3 | 31.3 |
| Maximum dry density ($\text{g}\cdot\text{cm}^{-3}$) | 1.913 | 1.518 |
| Uniformity coefficient | 11.7 | 1.7 |
| Curvature coefficient | 1.65 | 0.73 |
| Loss-on-ignition (%) | / | 14.67 |

Their particle size gradation curves are shown in Figure 2. The selected soil is silty with fine sand (silty soil). Figure 2 shows that the RM has poor particle gradation, fine particle content is as high as 88.83%.

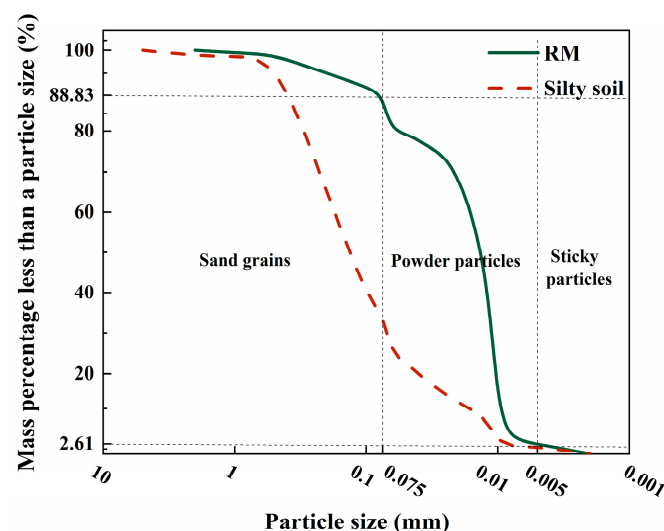


Figure 2. Gradation curve of RM and silty soil particles.

The main chemical compositions and contents of the silty soil and the RM are shown in Table 2. It can be seen that the content of SiO_2 , Al_2O_3 , and CaO in RM is more than 60%, which are the main components of alkali-activated cementitious materials.

Table 2. Main chemical composition of the test materials.

| Material | Al_2O_3 | SiO_2 | Fe_2O_3 | CaO | TiO_2 | K_2O | MgO | Na_2O | SO_3 | Others |
|------------|-------------------------|----------------|-------------------------|--------------|----------------|----------------------|--------------|-----------------------|---------------|--------|
| Silty soil | 9.58 | 67.89 | 5.97 | 3.04 | 2.86 | 1.75 | 2.82 | / | 0.46 | 5.63 |
| RM | 20.10 | 13.28 | 3.32 | 32.02 | 3.81 | 0.35 | 1.16 | 10.9 | / | 15.06 |

The cement used in the experiment is grade 42.5 ordinary Portland cement (P.O42.5) supplied by Henan Yongan Cement Co., Ltd. (Zhengzhou, China), with the quality indices shown in Table 3.

Table 3. Cement quality index.

| Specific Area (m ² ·kg ⁻¹) | Cl (%) | SO ₃ (%) | MgO (%) | Loss-on-Ignition (%) | Initial Setting (Time/min) | Final Setting (Time/min) | Stability |
|--|--------|---------------------|---------|-------------------------|-------------------------------|-----------------------------|-----------|
| 352 | 0.043 | 2.77 | 3.51 | 3.51 | 209 | 291 | qualified |

2.2. Test Methods

To study the strength characteristics and microscopic mechanism of P.O-RMS, compaction tests and UCS tests were conducted according to the Chinese Highway Geotechnical Test Procedure (JTG 3430–2020). Microscopic tests such as XRD, TG-DTG, and SEM were used to analyze the mechanism of strength formation and its variation in the P.O-RMS. Moreover, the glass electrode method and gamma-ray spectrometric survey were used to determine the environmental impact indices of P.O-RMS.

1.2.1 specimen preparation
The Chinese code for roadbed fillers of high-grade highways typically requires a 95% compaction degree (K) for UCS test specimens. The specimens' mass and water content ratio were determined according to the compaction test results. Cylindrical specimens of 50 mm in diameter and height were prepared by the static pressure method, and six identical specimens of each soil type were prepared for parallel testing. Thereafter, the specimens were wrapped with preservative film and put in a curing box at 20 °C temperature and 95% humidity. On the last day of curing, the specimens were soaked in water for 24 h for further use [14].

2.2.1. Compaction Test

The optimal water content (w_{op}) and the maximum dry density (ρ_{dmax}) of the P.O-RMS were determined using an indoor light compaction test according to ASTM standards [15]. Initially, the soil specimens were crushed to pass through a 5 mm sieve and dried for 12 h. Then, the specimens with five water content gradients were prepared in 2% increments, centered on the w_{op} that had been predicted using the liquid–plastic limit test results. The specimens were sealed with double PVC plastic bags for 10 h so that the water in the specimen would be uniformly distributed. Later, the soil specimen was divided into five layers for compaction, and each layer was compacted 27 blow times. After each compaction, the rough edges of the specimen's surface were repaired. Subsequently, the total mass of the compaction cylinder and the soil specimen was weighed, and the water content ratio of the central soil specimen was measured. Finally, according to the compaction test results, the w_{op} and ρ_{dmax} of the P.O-RMS were calculated.

2.2.2. Unconfined Compressive Strength Test

According to Test Methods of Soils for Highway Engineering (JTG 3430–2020), the UCS of the specimens was measured using a YYW-2 unconfined compressive strength instrument. The surface water of the cured specimen was wiped off before the UCS test, and the axial strain rate was measured at 1 mm/min during the test. The data of the dial indicator were recorded during the test, and the failure trend and morphology of the specimen were observed. The stress–strain relationship curve was drawn according to the test data. The UCS calculation formulas are shown in (1)–(3).

$$\varepsilon_1 = \frac{\Delta h}{h_0} \times 100 \quad (1)$$

where, ε_1 is the axial strain (%), h_0 is the initial height of the specimen (cm), and Δh is the axial deformation (cm).

$$A_a = \frac{A_0}{1 - \varepsilon_1} \quad (2)$$

where, A_a is the fracture area of the calibrated specimen (cm²) and A_0 is the initial area of the specimen (cm²).

$$\sigma = \frac{10CR}{A_a} \quad (3)$$

where, σ is the axial pressure (kPa), C is the calibration coefficient of the dynamometer (N/0.01 mm), R is the reading of the dial indicator (0.01 mm), and 10 is the unit conversion coefficient.

2.2.3. Microstructural Test

Representative test specimens were selected for microstructure and hydration product analysis. Before the XRD test, the specimens were vacuum dried, then crushed through a 0.15 mm sieve. A German Bruker D8 Advance X-ray diffractometer was used in the test. The test parameters were set as follows: the working voltage is 20 to 60 kV, the working current is 10 to 300 mA, the constant step size is 0.002° to 90°, the scanning rate is 0.002 to 100°/min, and 2 θ the angle test range is 5° to 80° [16].

The specimens were vacuum dried and crushed, then processed through a 0.15 mm sieve before the TG-DTG test. Then, 15 mg of the treated specimens were weighed and placed in an alumina crucible for the test. A NETZSCH STA 499 F5 synchronous thermal analyzer was used in the test. The test parameters were set as follows: the gas output pressure is 0.04 MPa, the temperature rise rate is 10 °C/min, and the temperature range is 0 to 1000 °C [17].

The fresh sections (about 1 cm²) of typical parallel specimens in the UCS test were used as the specimen for the SEM test [18]. The specimen is freeze-dried in liquid nitrogen and spray-gold so that the specimen achieves a completely dry state and is ready for use. Finally, SEM images with a magnification of 10,000 times were obtained using a SU8100 series Hitachi High-Tech ultra-high resolution field emission scanning electron microscope.

2.2.4. Environmental Index Test

The glass electrode method [19] was used to test the P.O-RMS' corrosion. The horizontal vibration method prepared the leaching solution before the test. The specimen was mixed with water at a solid–liquid ratio of 1:10. It then oscillated for 8 h and stayed for 16 h before the filter fluid was finally collected. In the experiment, the leaching solution was poured into the beaker and put into the agitator, and the liquid level was higher than the electrode's sensitive element. The electrode was inserted into the beaker, stirred uniformly, and the was read pH after the reading was stable.

A leaching test [20,21] was performed to detect the leaching concentration of P.O-RMS heavy metals. The first step involved drying the 9.5 mm particle specimen, followed by the obtainment of a specimen of 200 g. Then, the sulfuric acid and nitric acid leaching agent was added at a solid–liquid ratio of 1:10. It was then passed through a 0.6 μ m filter membrane after concussion. It was acidified with nitric acid to pH < 2 before storage. Finally, the leaching concentrations of different heavy metal ions were determined by spectrophotometry.

A gamma-ray spectrometric survey was used to study the radioactivity level of the P.O-RMS. By detecting the γ -ray produced by a certain radionuclide, the corresponding γ -ray energy spectrum can be obtained. Thus, the total radioactivity and content of the nuclide were obtained. Before the test, the specimens were crushed and sealed. The radioactivity of the specimen was measured after 7 d [22]. An FP-90041 low background gamma-ray spectrometric survey was used in the experiment. It has an extended uncertainty of less than 15%, an energy resolution of less than 7%, and a measurable nuclide activity range of 10 to 2000 Bq.

2.3. Experimental Scheme

To investigate the effects of the proportion and the curing age on the strength of P.O-RMS, the specimens with different proportions and curing ages were prepared for testing, followed by a comparative analysis of the results. The experimental scheme and selected test specimens were numbered as shown in Table 4. The amount of RM and cement was determined according to the percentage of the dry mass of silty soil. The cement content ($W_{P.O}$) was 6%, 9%, and 12% while the RM content (W_{RM}) ranged from 0% to 23%. The curing age is 7 d, 28 d, and 90 d. A total of 45 soil specimens were set up for the mechanical test, and 6 specimens of each soil were prepared. Additionally, the representative specimens of the UCS test results were used for the microscopic test. For the convenience of description, specimens with different mix proportions otherwise expressed in corresponding English abbreviations, such as 6% P.O42.5 and 14% RM, are expressed as 6% $W_{P.O}$ + 14% W_{RM} .

Table 4. Experimental scheme.

| Type of Test | Cement Content ($W_{P.O}$) (%) | RM Content (W_{RM}) (%) | Curing Age (d) | Specimen Number |
|------------------|----------------------------------|-----------------------------|----------------|-----------------|
| Mechanical test | 6, 9, 12 | 0, 14, 17, 20, 23 | 7, 28, 90 | \ |
| | 12 | 20 | | R-1 |
| | | 20 | 28 | R-2 |
| Microscopic test | 9 | 23 | | R-3 |
| | | 0 | | R-4 |
| | 9 | 20 | 90 | R-5 |

3. Results and Analysis

3.1. Raw Materials

From the XRD pattern of Figure 3, it can be seen that the main phase of the silty sand is quartz and bauxite (Al_2O_3). Moreover, the RM's main phases are quartz, corundum, hematite, and complex minerals.

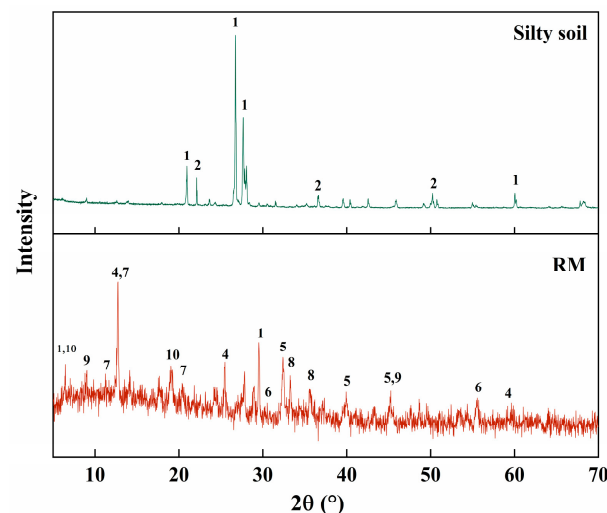


Figure 3. XRD patterns of particle size distribution curves of RM and silty soil (1 Quartz- SiO_2 ; 2 Aluminum- Al_2O_3 ; 3 Sodium Silicate- Na_4SiO_4 ; 4 Corundum, syn- Al_2O_3 ; 5 Katoite, $Sirich-Ca_3Al_2SiO_4(OH)_8$; 6 Lime, syn- CaO ; 7 Cancrinite- $Na_6Ca_2Al_6Si_6O_{24}Ca_{32}H_2O$; 8 Hematite- Fe_2O_3 ; 9 Calcium Silicate Hydrate- $Ca_2SiO_4 \cdot xH_2O$; 10 Chamosite- $(Fe,Al,Mg)_6(Si,Al)_4O_{10}(OH)_8$).

The pollution of RM in the environment is mainly exemplified by strong alkalinity, heavy metal leaching toxicity, and radioactivity. The RM in this research study exhibited a

pH of 11.71, indicating that it is highly alkaline. Leaching concentrations of various heavy metal ions in RM are shown in Figure 4, which shows that the toxic leaching concentration of each component in the RM is below the limit value. This means that it should be categorized as Class II general industrial solid waste, but is not hazardous solid waste [23].

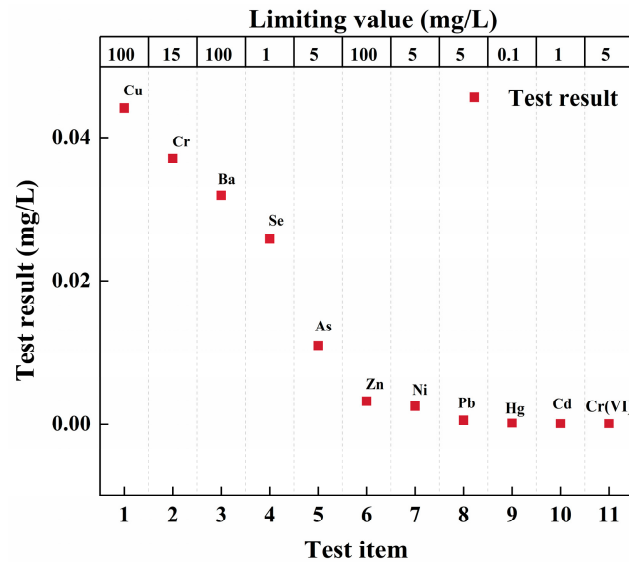


Figure 4. Heavy metal leaching concentration of RM.

A gamma-ray spectrometric survey was used to study the radioactivity level of the RM. The specific radioactivity of radium-226 (^{226}Ra), thorium-232 (^{232}Th), and potassium-40 (K40) in the RM were found to be $508 \text{ Bq}\cdot\text{kg}^{-1}$, $265 \text{ Bq}\cdot\text{kg}^{-1}$, and $1050 \text{ Bq}\cdot\text{kg}^{-1}$, respectively. Therefore, the internal irradiation index (I_{Ra}) of RM is 2.54, and the external irradiation index (I_{r}) is 2.63.

3.2. Compaction Characteristic

The compaction curve of P.O-RMS with different W_{PO} is shown in Figure 5. The compaction curve moves to the lower right with the increase of W_{RM} and becomes steeper after the peak. The dry density decreases considerably with increasing water content, while the soil's sensitivity to water increases.

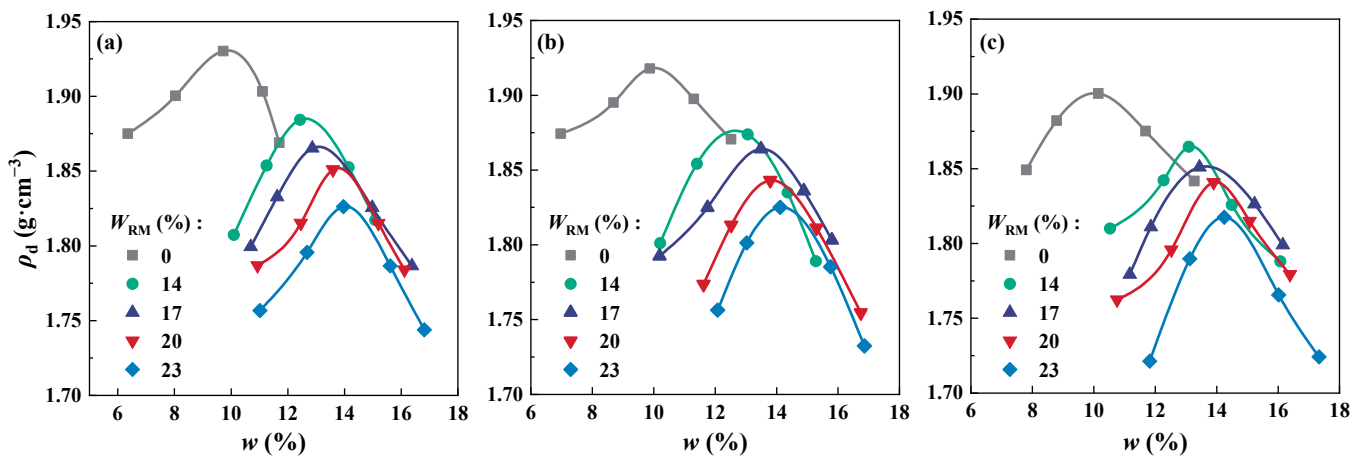


Figure 5. Compaction curve: (a) $W_{\text{PO}} = 6\%$; (b) $W_{\text{PO}} = 9\%$; (c) $W_{\text{PO}} = 12\%$.

The curves of ρ_{dmax} and w_{op} with different W_{RM} are plotted as shown in Figure 6. It can be seen that with the growth of W_{RM} , w_{op} increases, and ρ_{dmax} decreases. The same applies to W_{PO} . This phenomenon is attributed to the fine particles in both RM and P.O42.5.

As W_{RM} and $W_{P.O}$ increase, not only does the content of fine particles in soil increase, but its water-holding capacity increases as well. The encapsulation of coarse particles by fine particles results in the destruction of the soil skeleton structure, leading to a reduction in dry density. Additionally, the cement undergoes hydration in the alkali environment provided by RM to form a binding material, thereby resulting in poor pore-filling.

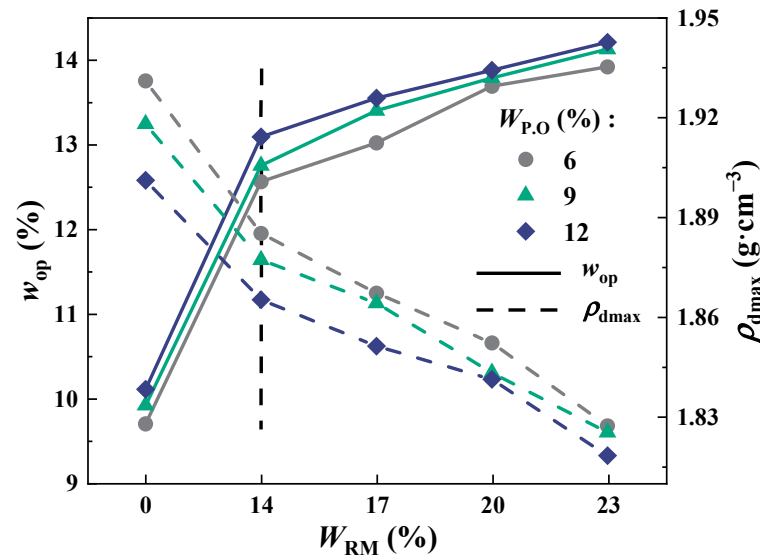


Figure 6. Optimal water content and maximum dry density.

3.3. Unconfined Compressive Strength

3.3.1. Axial Stress–Strain Curve

Figure 7 shows the axial stress–strain curves (σ – ϵ curves) of P.O-RMS specimens at different curing ages and proportions. Because the development trends of σ – ϵ curves of $W_{RM} = 14\%$ and 17% specimens are the same as that of $W_{RM} = 20\%$ and 23% specimens. Therefore, only analyzes the σ – ϵ curves of specimens with the smallest, largest, and reduced stress peaks in the five RM ratios (i.e., $W_{RM} = 0\%$, 20% , and 23%). In Figure 7, peak points and strain softening characteristics can be observed obviously, i.e., when the stress of the specimen reaches the peak strength, it will quickly decrease to a lower level. The comparison indicates that the variation trend of the P.O-RMS specimens' σ – ϵ curves exhibit three different development trends, namely "a", "b", and "c", as shown in Figure 8. The change trends of the σ – ϵ curves are analyzed by combining Figures 7 and 8.

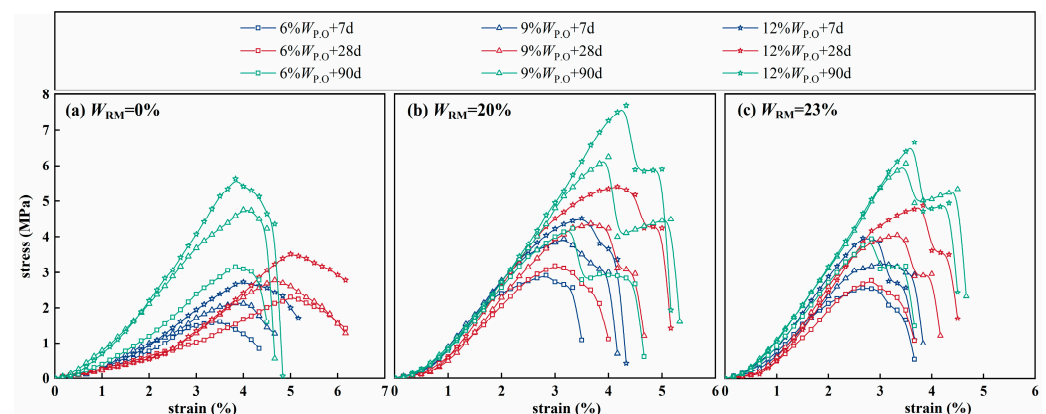


Figure 7. Stress–strain relationship curve: (a) $W_{RM} = 0\%$; (b) $W_{RM} = 20\%$; (c) $W_{RM} = 23\%$.

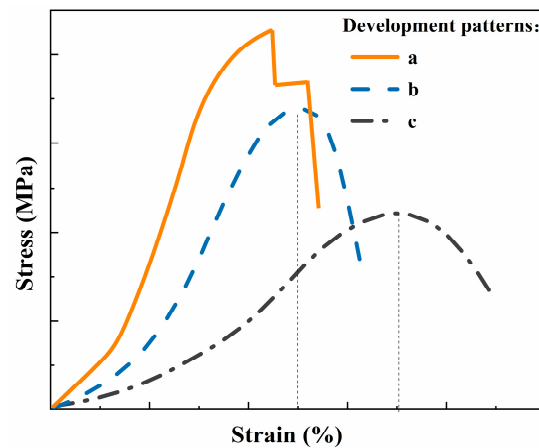


Figure 8. Development trends of stress–strain relationship curve.

The σ – ε curve of the specimen with $W_{RM} = 0\%$ shows the “b” development trend at 90d (Figure 7a). Conversely, when $W_{RM} \neq 0\%$, the specimen’s σ – ε curve mainly presents two distinct development trends, “a” and “b”, at 28 d and 90 d (Figure 7b,c). Furthermore, the σ – ε curve indicates the “b” development trend at 7 d. The σ – ε curve can be divided into three stages: initial loading, elastic deformation, and failure. Some pores inside the specimen are rapidly compressed during the initial loading stage. In this stage, the strain grows rapidly, but the stress changes slowly. Nevertheless, the duration of this stage is short, due to the better structure of the P.O-RMS. As the load increases, the specimen enters the elastic deformation stage, where its structural strength plays a major role. At this stage, the stress grows rapidly while the strain changes slowly. This phenomenon is characterized by a linear growth trend on the σ – ε curve. This stage lasts for a longer time, which is the main stage in the elastic deformation process of the specimen. Finally, the failure stage occurs. There is a short plastic deformation stage before the specimen is completely destroyed. When the soil starts to break down, the strain grows considerably, and obvious cracks appear on the surface of the specimen. When the stress reaches its peak, it gradually decreases with the further development of strain, and the specimen completely fails.

The σ – ε curves of specimens with $W_{P.O} > 6\%$ exhibit an “a” development trend at 7 d and 28 d of curing. In this case, the residual stress plays a vital role in the failure stage (Figure 7b,c). After the stress reaches the peak and rapidly drops to a lower level, the declination rate of stress slows down. It even rises with the increase of strain ($W_{P.O} = 9\%$ at 90 d). This observation is attributed to the increased hydration reaction at long curing ages that improves the structure’s bond strength. The complete failure of the specimen requires multiple shear surfaces to run through together. Overall, the specimens with $W_{RM} \neq 0\%$ have a small elastic-plastic deformation, showing brittle failure characteristics.

In Figure 7a, the σ – ε curves of the specimens with $W_{RM} = 0\%$ exhibit a “c” development trend when the curing ages are 7 d and 28 d. This trend is mainly divided into plastic deformation and plastic yield stages. In the plastic deformation stage, the stress increases slowly with the rapid development of strain. When the strength achieves its peak, the specimen enters the plastic yield stage. The specimen gets destroyed, but the strength reduction rate is relatively slow. The σ – ε curve is relatively flat as a whole, and the plastic deformation is large, showing certain plastic failure characteristics. Since the hydration products in the specimens with $W_{RM} = 0\%$ and short curing age are relatively less, the sliding and dislocation of particles play a partial role in the failure process of the specimens. Therefore, the addition of RM is beneficial to the P.O42.5 hydration reaction and the improvement of the structural strength of the specimen. The σ – ε curve of the specimens with $W_{RM} = 0\%$ exhibits a “b” development trend when the curing age is 90 d. Furthermore, the stress grows faster with increasing strain. This is accompanied by a reduction in the plastic deformation of the soil, resulting in a brittle failure behavior.

3.3.2. Deformation Characteristic

Failure strain (ε_f) reflects the deformation characteristics of the soil; the greater the ε_f , the stronger the toughness. The ε_f is the strain corresponding to the peak stress of the specimen. The variation curve of ε_f with W_{RM} is shown in Figure 9.

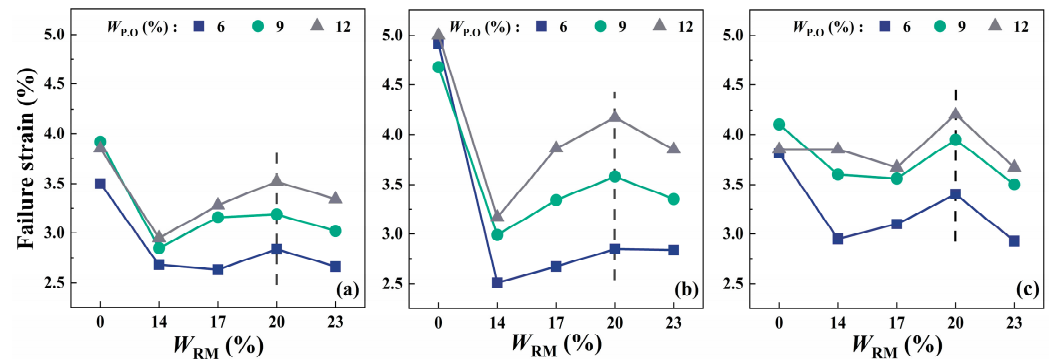


Figure 9. Variation curve of failure strain and RM content (W_{RM}): (a) 7 d; (b) 28 d; (c) 90 d.

It can be seen that when the curing age is 7 d and 28 d, under the same $W_{P,O}$, the specimen with $W_{RM} = 0\%$ has the largest ε_f . However, when W_{RM} increases from 14% to 23%, ε_f first increases and then decreases. In addition, the ε_f at $W_{RM} = 20\%$ is the turning point of the curve in this region. Although RM has an adverse effect on the ε_f of the specimen at the initial stage of curing, with the increase of W_{RM} and curing age, the adverse effect gradually decreases. For example, at 28 d curing age (Figure 9b), when $W_{P,O} = 12\%$, ε_f of $W_{RM} = 14\%$ is 3.2%, with the growth of W_{RM} to 20%, ε_f increases to 4.2%. Moreover, when W_{RM} increases to 23%, ε_f decreases to 3.8%. At 90 d (Figure 9c), the ε_f of the specimen with $W_{RM} \neq 0\%$ is still the largest when $W_{P,O} = 12\%$. For example, when $W_{P,O} = 12\%$ and W_{RM} is 14%, 17% and 23%, the ε_f of the specimen is 3.85%, 3.67% and 3.66%, respectively. Meanwhile, when $W_{RM} = 20\%$, the peak of ε_f is 4.2%. It is worth noting that the failure strain of $W_{RM} = 0\%$ and $W_{RM} = 14\%$ specimens is the same.

Further analysis of the P.O-RMS' deformation characteristics is performed using the deformation coefficient (E_{50}). This parameter refers to the secant modulus at the point corresponding to half of the failure strain in the σ - ε curve, which reflects the ability of the specimen's deformation resistance. Generally, the greater of E_{50} , the stronger the deformation resistance [24]. The variation curve of E_{50} with W_{RM} is shown in Figure 10.

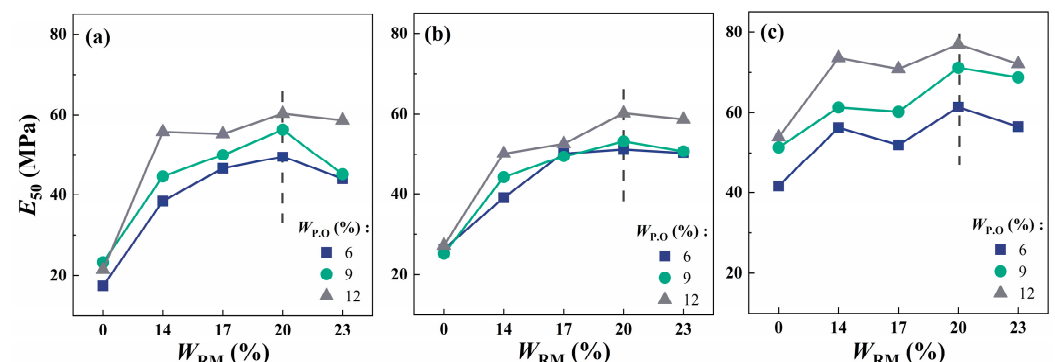


Figure 10. Variation curve of E_{50} and W_{RM} : (a) 7 d; (b) 28 d; (c) 90 d.

It can be observed that the E_{50} is small when $W_{RM} = 0\%$, hence the resistance to deformation is weak. Moreover, it can be noticed that the E_{50} increases rapidly after adding RM, and the resistance to deformation is enhanced. The E_{50} reaches its peak at $W_{RM} = 20\%$ regardless of the curing ages. Because RM improves the P.O42.5 hydration, the specimen forms a high-strength brittle skeleton, and the slight deformation only occurs under large stresses, which shows strong deformation resistance.

Comparing Figure 9 to Figure 10, it can be observed that when $W_{RM} \neq 0\%$, the specimen with $W_{RM} = 20\%$ has the best toughness and deformation resistance.

3.3.3. Strength Characteristic

Figure 11 shows the UCS of the P.O-RMS. It can be observed that compared to the UCS of P.O42.5 only, the incorporation of RM significantly improves the UCS of the specimen. The RM provides an alkaline environment that improves the P.O42.5 hydration reaction, resulting in a rapid increase in the strength of the overall cementitious system. Therefore, the UCS of the specimen with $W_{RM} = 0\%$ is the smallest (Figure 11a).

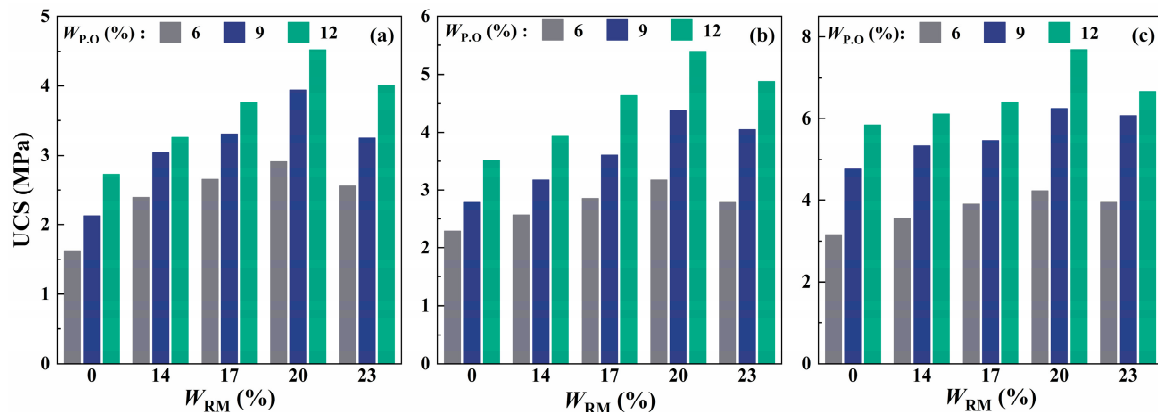


Figure 11. UCS: (a) 7 d; (b) 28 d; (c) 90 d.

At the same curing age and W_{RM} , with the increase of W_{PO} , the UCS of P.O-RMS increases gradually. When the W_{PO} is constant, the UCS of the P.O-RMS increases first and then decreases with the increase of W_{RM} . As shown in Figure 11b, when W_{RM} increases from 0% to 20% at $W_{PO} = 9\%$, the P.O-RMS' UCS increases from 2.78 MPa to 4.37 MPa, but when W_{RM} increases to 23%, the UCS decreases to 4.05 MPa. The reason for this phenomenon is that in the process of P.O42.5 hydration, due to the presence of excessive alkali, the precipitated NaOH and KOH react with active substances in the soil (such as SiO_2) alkali-silica reaction. This leads to a decrease in the output of CSH and other gels, and alkali-based silicate gel formed expands by water absorption, which destroys the specimen's skeleton structure. In addition, the unhydrated RM particles are adsorbed around the hydration products, which reduces the compactness of the soil. Therefore, it is crucial to control the W_{RM} in P.O-RMS.

To analyze the relationship between the strength and deformation characteristics of P.O-RMS, the relationship curves between the UCS and deformation characteristic parameters (ϵ_f and E_{50}) are given, as shown in Figure 12.

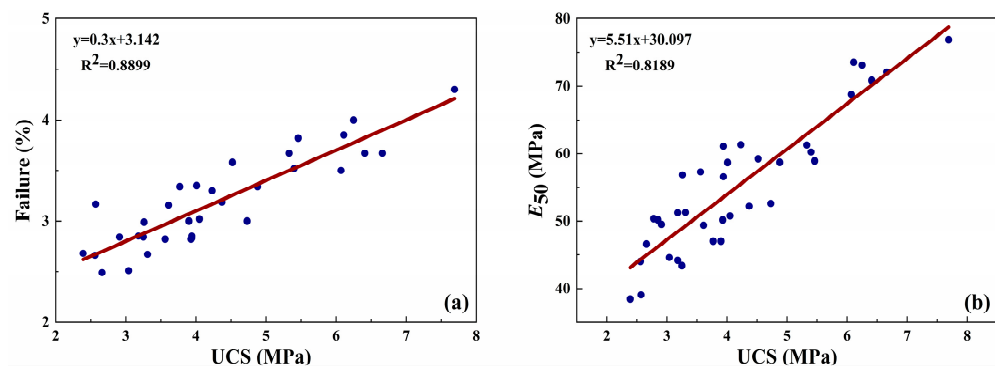


Figure 12. UCS and deformation characteristic parameters: (a) UCS and ϵ_f ; (b) UCS and E_{50} .

It can be seen in Figure 12a that as the UCS of the P.O-RMS increases, the ϵ_f generally shows an upward trend, which indicates that the P.O-RMS has higher strength and tough-

ness. However, the variation of ε_f is small and within the range of 1.5%. Figure 12b shows that E_{50} increases significantly with the increase of the UCS of the P.O-RMS, indicating that the higher the strength of the P.O-RMS, the greater the resistance to deformation. The above results show that the deformation characteristics of P.O-RMS are good when its strength is high ($W_{RM} = 20\%$).

When the $W_{RM} = 20\%$ and W_{PO} is 6%, 9%, and 12%, the UCS of P.O-RMS is 2.91 MPa, 3.94 MPa, and 4.52 MPa at 7 d, respectively. According to the UCS standard of cement stabilized materials at 7 d in China's Technical Rules for Highway Pavement Base Construction (JTGT F20-2015) [25], when a mix of 6% $W_{PO} + 20\% W_{RM}$ is added, it meets the lower limit requirement of grade II highway base strength (>2 MPa). Adding 9% $W_{PO} + 20\% W_{RM}$ can meet the lower limit requirements (>3 MPa) of highway and primary highway base strength. Therefore, it is possible to use $W_{RM} = 20\%$ and a suitable W_{PO} to be the requirements of different highway grades.

3.3.4. Failure Modes

The failure modes of specimens under unconfined compressive conditions are closely related to their strength characteristics. There are three main failure modes of P.O-RMS under different UCSs. Figure 13 shows the representative photos of the failure modes in the UCS test.

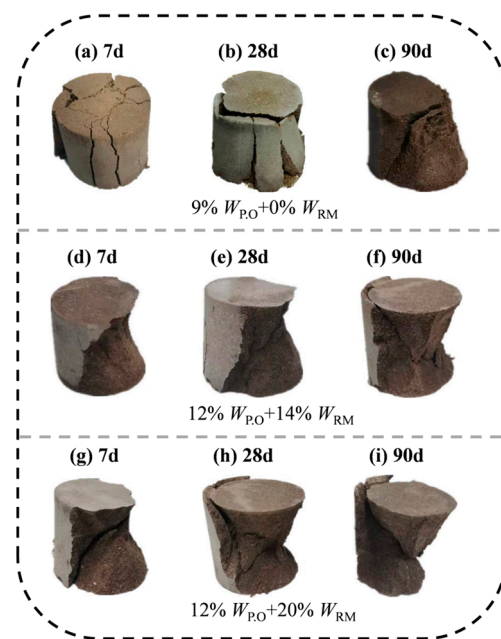


Figure 13. Typical failure pattern of P.O-RMS: (a) 9% $W_{PO} + 0\% W_{RM}$ (7 d); (b) 9% $W_{PO} + 0\% W_{RM}$ (28 d); (c) 9% $W_{PO} + 0\% W_{RM}$ (90 d) (d) 12% $W_{PO} + 14\% W_{RM}$ (7 d); (e) 12% $W_{PO} + 14\% W_{RM}$ (28 d); (f) 12% $W_{PO} + 14\% W_{RM}$ (90 d); (g) 12% $W_{PO} + 20\% W_{RM}$ (7 d); (h) 12% $W_{PO} + 20\% W_{RM}$ (28 d); (i) 12% $W_{PO} + 20\% W_{RM}$ (90 d).

The UCS of 9% $W_{PO} + 0\% W_{RM}$ at 7 d and 28 d and 12% $W_{PO} + 14\% W_{RM}$ at 7 d are 2.13 MPa, 3.04 MPa, and 3.26 MPa, respectively (Figure 13a,b,d). The specimen's strength is weak, which is mainly characterized by tension cracking damage. There is no specific shear failure surface upon specimen collapse, but the overall or local tensile cracks, and the longitudinal cracks develop until they run through, leading to the failure of the specimen. The incomplete hydration reaction at low strength produces less cementitious materials and more pore content, resulting in a weak connection between soil particles and a low density. Under compressive stress, the periphery of the specimen is subjected to horizontal tension causing vertical cracks to appear first at the weak surface. With the further stress increase, slip failure occurs at the contact junction of the unit body, longitudinal cracks develop and

penetrate, and the entire or part of the specimen collapses. However, the failure process of the specimen is relatively gentle, showing certain plastic failure characteristics.

The gels generated by the hydration reaction in the specimen increase with the extension of the curing age or the increase in W_{RM} , so the strength of the specimen increases and the shear failure occurs upon total collapse. For instance, the UCS of 9% W_{PO} + 0% W_{RM} at 90 d, 12% W_{PO} + 14% W_{RM} at 28 d, and 12% W_{PO} + 20% W_{RM} at 7 d specimens are 4.75 MPa, 3.97 MPa, and 4.52 MPa, respectively (Figure 13c,e,g). The reinforcement of cementation between structural units results in a higher overall strength of the structure. As compression stress intensifies, the weak surface of the specimen cracks first and develops longitudinally. However, the overall structural strength is not affected. As the stress increases, the displacement occurs at a weak cementation. The shearing damage surface is gradually formed by oblique cracks. The failure of the specimen is mainly concentrated in the shear band.

The specimen presents a conical failure mode with a further increase in strength. For example, the UCS of 12% W_{PO} + 14% W_{RM} at 90 d and 12% W_{PO} + 20% W_{RM} at 28 d and 90 d specimens are 6.11 MPa, 5.4 MPa, and 7.69 MPa, respectively (Figure 13f,h,i). In this case, the connection of structural units is strong and the anisotropy is enhanced, which limits the crack propagation. As compressive stress increases, the specimen continues to experience shear failure. Despite this, the primary shear band present in the specimen fails to fully penetrate the entire structure. Ultimately, the specimen only fails when multiple shear bands and cross cracks develop simultaneously throughout. As a result of the aforementioned failure mechanism, the σ - ε curve of the $W_{RM} \neq 0\%$ specimen exhibits a significant residual stress effect at 90 d. In addition, due to the large bond strength between the units, the specimen can withstand large compressive stress, showing strong deformation resistance.

3.4. Environmental Index Parameters

The environmental impact assessment of P.O-RMS with $W_{RM} = 20\%$ is investigated in this study. For the environmental index test, the specimens of 6% W_{PO} + 20% W_{RM} at 28 d were selected, taking into account the most unfavorable conditions. Compared with pure RM, the environmental indices of the P.O-RMS are improved. The pH of the P.O-RMS is 8.62, which is 3.1 lower than that of the pure RM. The test reduction in the toxic leach concentration of P.O-RMS is shown in Figure 14a.

It can be seen that the fluoride leaching concentration decreased by 51.1% from 0.9 to 0.44 mg/L. Combining all testing items, the average decrease in the toxic leachate concentration is 91%.

Radioactivity indicators of RM and P.O-RMS are shown in Figure 14b. The specific activities of radionuclides ^{226}Ra , ^{232}Th , and K40 in the P.O-RMS are 103 Bq·kg⁻¹, 52 Bq·kg⁻¹, and 198 Bq·kg⁻¹, respectively, with $I_{Ra} = 0.52$ and $I_r = 0.53$, meeting the requirements of China's radionuclides in construction materials ($I_{Ra} \leq 1$; $I_r \leq 1$). In conclusion, all environmental indicators of P.O-RMS with $W_{RM} = 20\%$ meet the requirements of the Chinese specifications. Thus, P.O-RMS has the potential to be employed as a sustainable construction material for roadbeds.

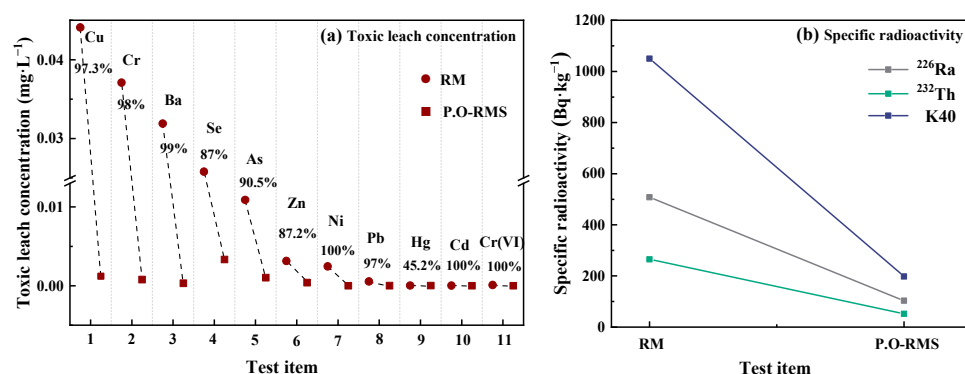


Figure 14. Environmental Index Parameters of RM and P.O-RMS: (a) Toxic leaching concentration; (b) Specific radioactivity.

3.5. Micro-Mechanism

The micro-test specimens were selected based on the UCS test results, and their hydration products and micro-morphology were characterized by XRD, TG-DTG, and SEM tests. In this section, the effects of curing age, $W_{P.O}$, and W_{RM} on the strength change of P.O-RMS at the micro level were analyzed.

3.5.1. X-ray Diffraction Analysis

Figure 15 shows the P.O-RMS' XRD patterns. It can be seen that there are primary minerals in the P.O-RMS with $W_{RM} \neq 0\%$, such as hematite, hydrogrossular, and cancrinite. Primary minerals are less active and do not easily participate in hydration reactions.

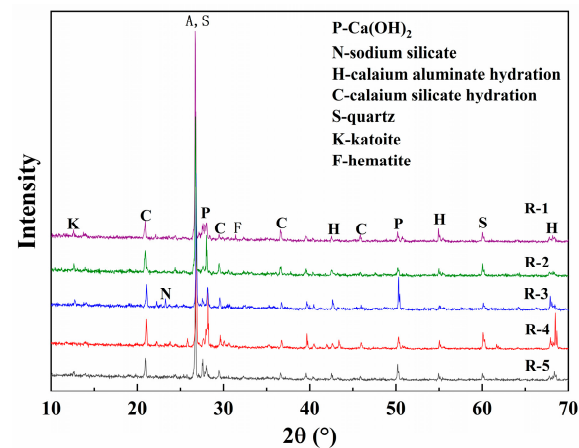
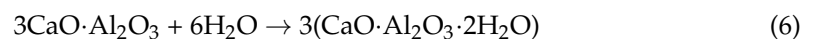
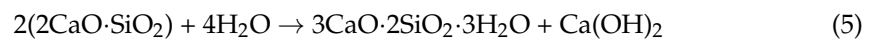
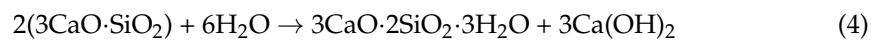


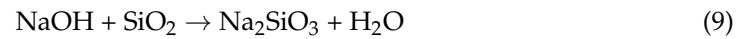
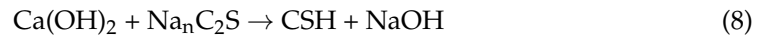
Figure 15. XRD pattern of P.O-RMS.

This study primarily focuses on the analysis of the key hydration products that affect the unconfined compression strength (UCS). Under the combined action of P.O42.5 hydration and RM auxiliary excitation, the hydration products in the P.O-RMS are mainly $\text{Ca}(\text{OH})_2$ and amorphous cementitious materials (such as CSH and CAH). The alkali environment promotes the depolymerization of Si-Al tetrahedron in P.O42.5 and regenerates cementitious products and $\text{Ca}(\text{OH})_2$. The $\text{Ca}(\text{OH})_2$ generated by P.O42.5 hydration has a destructive effect on the silica–oxygen and aluminum–oxygen bonds of some active minerals in RM, thus producing Si and Al. In the P.O-RMS, $\text{Ca}(\text{OH})_2$ gradually increases with the hydration reaction of P.O42.5, and Ca^{2+} polymerizes with Si and Al to produce gel products such as CSH. The gel products are the reason for the strength improvement of P.O-RMS specimens. The main reaction equations [26,27] are shown in (4)–(7).



From Figure 15, it can be found that the characteristic peak of the R-4 specimen at 28.3° (the main characteristic peak of $\text{Ca}(\text{OH})_2$) is larger. This illustrates that $\text{Ca}(\text{OH})_2$ does not react sufficiently at $W_{RM} = 0\%$, and less gelatinous material is produced. Consequently, the soil's strength is lower in comparison. The characteristic peak of sodium silicate gel was detected at 23.3° in the R-3 specimen, indicating the presence of an alkali–silicate reaction at this point. As a result of RM's high alkalinity, the hydration process of P.O42.5 causes precipitation of NaOH and KOH, which react with Si to generate alkali silicate gel. The

water absorption expansion of alkali silicate gel can damage the soil structure and decrease structural strength. Taking sodium silicate gel as an example for a detailed explanation. While P.O42.5 hydration produces $\text{Ca}(\text{OH})_2$, CSH, and other gels, a large amount of free Ca^{2+} is replaced by Na^+ in RM, and the resulting NaOH reacts chemically with SiO_2 in the soil to produce Na_2SiO_3 gel. The main reaction equations are shown in (8) and (9).



The alkali–silicate reaction of NaOH with SiO_2 affects the reaction of the calcium base with the active substance. The gel materials produced can result in localized soil expansion, disrupt the soil structure, and ultimately lead to a decrease in UCS for P.O-RMS. The strength of P.O-RMS with $W_{\text{RM}} = 23\%$ reduced; hence the W_{RM} should be controlled when using it.

3.5.2. Thermogravimetric-Differential Thermal Analysis

The cementitious products and $\text{Ca}(\text{OH})_2$ content in the P.O-RMS reflect the microscopic mechanism of soil strength change. Figure 16 shows the TG-DTG analysis profiles of P.O-RMS microscopic test specimens.

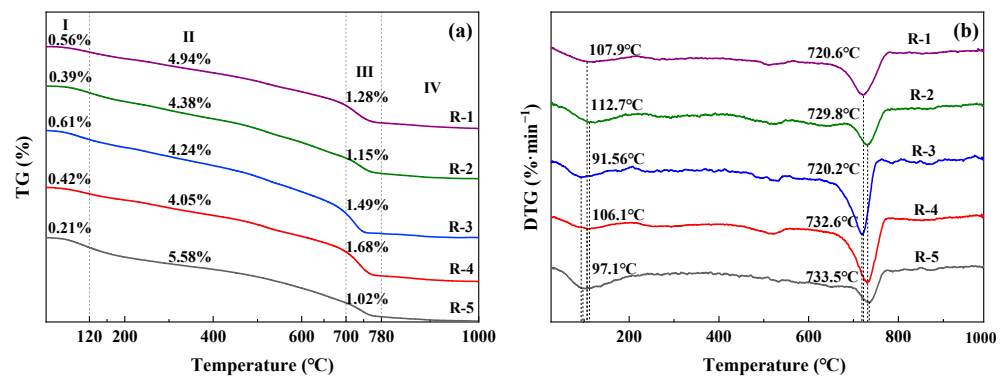


Figure 16. TG-DGT: (a) TG; (b) DGT.

As seen in Figure 16, the weight loss of the specimen can be divided into four stages with the increase in temperature. The onset of Stage I weightlessness, manifesting at 120 °C, can be primarily attributed to the removal of free water in the soil. Free water content is determined by w_{op} , hydration reaction degree, and curing age. The maximum weight loss rate was 0.61% (R-3) in stage I, indicating high free water content in the soil. This phenomenon can be attributed to the strong water retention capability of the R-3, coupled with excessive alkalinity that impedes a hydration reaction.

Stage II (120 °C–700 °C) is relatively uniform and gentle. In this stage, weight loss occurs mainly due to the dehydration and decomposition of the hydration products (such as CSH, etc.) and the removal of bound water from some minerals. The weight loss rate of stages I and II reflects the content of hydration products. In Stage II, a comparison of weight loss rates between soil specimens with varying curing ages (R-2 and R-5) reveals that the hydration products of these specimens increase with an extended duration of curing, resulting in an elevation in strength. Meanwhile, when comparing weight loss rates of soil specimens possessing different W_{RM} (R-2, R-3, and R-4) during Stage II, it was noted that the lowest rate of weight loss occurred for R-4 at 4.02%. Further analysis revealed that the presence of RM (R-2 and R-3) facilitated greater production of hydration products, thus accounting for their higher UCS compared to R-4. The R-2 specimen has greater weight loss than the R-3. Although R-3 has gel production, it is less than R-2, indicating that excessive alkaline and RM particles inhibit hydration reactions.

In stage III (700 °C–780 °C), weight loss is dominated by $\text{Ca}(\text{OH})_2$ decomposition. The low weight loss rate of $\text{Ca}(\text{OH})_2$ indicates that $\text{Ca}(\text{OH})_2$ generated by P.O42.5 hydration is consumed more. The mechanism is that Ca^{2+} reacts fully with Si and Al in the soil to generate more hydration products. The maximum weight loss in stage III was 1.68% (R-4), indicating that $\text{Ca}(\text{OH})_2$ was not consumed in the specimens (R-4) without RM, and the specimens had fewer hydration products, resulting in lower strength. The weight loss rate of $\text{Ca}(\text{OH})_2$ in R-2 is less than that of R-3, which further shows that the hydration reaction of R-2 ($W_{\text{RM}} = 20\%$) is the most sufficient.

After 780 °C, the IV stage of weight loss is initiated, the structure of the stable aluminosilicate in the RM is disrupted in this stage, and some minerals begin to decompose, such as the decarbonization of cancrinite and decomposition of sodium carbonate [28–30].

3.5.3. Scanning Electron Microscopy

Figure 17 depicts the SEM images of the P.O-RMS microscopic test specimens at 10,000 \times magnification. In conjunction with Figure 17 and XRD data, it is clear that the primary hydration products of P.O-RMS are CSH and $\text{Ca}(\text{OH})_2$. At 28 d, the hydration products of 9% $W_{\text{P.O}}$ + 0% W_{RM} specimens are mainly long strip CSH and irregular sheet-like $\text{Ca}(\text{OH})_2$. This phenomenon is consistent with the XRD and TG-DGT results.

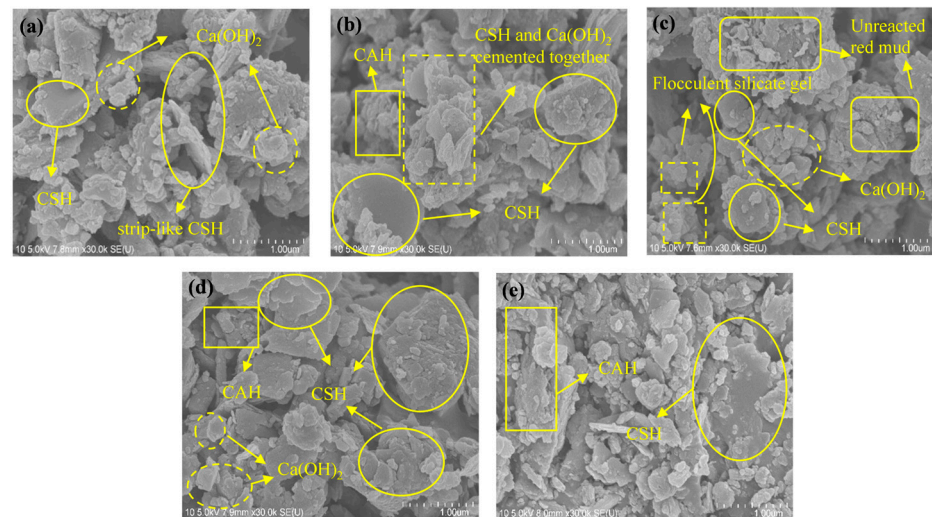


Figure 17. SEM images of P.O-RMS: (a) 9% $W_{\text{P.O}}$ + 0% W_{RM} (28 d); (b) 9% $W_{\text{P.O}}$ + 20% W_{RM} (28 d); (c) 9% $W_{\text{P.O}}$ + 23% W_{RM} (28 d); (d) 12% $W_{\text{P.O}}$ + 20% W_{RM} (28 d); (e) 9% $W_{\text{P.O}}$ + 20% W_{RM} (90 d).

Figure 17a indicates that the strip-like CSH is caused by insufficient hydration of P.O42.5. Furthermore, the cementing strength is weak and cannot completely fill the gap, resulting in a decrease in the strength of the soil. Furthermore, the insufficient reaction of $\text{Ca}(\text{OH})_2$ generated during cement hydration results in an excess accumulation of $\text{Ca}(\text{OH})_2$ within the soil. The sheet-like $\text{Ca}(\text{OH})_2$ is smaller in shape and grows haphazardly between the gels compared to the strip-like CSH, thus affecting the overall structural stability.

As seen in Figure 17b, the overall structure of the soil is dense, with only some tiny pores when $W_{\text{RM}} = 20\%$. The CSH in the soil is flat in shape, and some laminar flow-like CAH is produced. This gel has a large coating area and strong cementation ability. It can effectively fill the pores in the soil and create a denser microstructure. In addition, the content of $\text{Ca}(\text{OH})_2$ in soil decreased significantly, and no distinct residual RM particles were observed. This indicates that more $\text{Ca}(\text{OH})_2$ reacted with active substances in RM, which was consistent with the results of the TG-DGT test. A small amount of flake $\text{Ca}(\text{OH})_2$ and CSH intercalated and filled the structural pores to form a denser structure without adversely affecting the soil structure. As a result of the aforementioned factors, the UCS of P.O-RMS is the maximum when $W_{\text{RM}} = 20\%$.

When the W_{RM} increased to 23% (Figure 17c), there was flake CSH in the soil, but its area was significantly smaller than that when $W_{RM} = 20\%$. Furthermore, alkali–silica gel flocculent precipitate (Na_2SiO_3 , etc.) was also detected. These phenomena were consistent with the SEM and TG-DGT test results. Numerous unhydrated RM particles and $Ca(OH)_2$ in the soil, demonstrating that excessive W_{RM} cannot fully react with $Ca(OH)_2$ in P.O42.5, and will weaken the structural strength. According to Figure 17c, the overall structure appears to be relatively loose at this stage. This phenomenon can be attributed to the weak binding between unhydrated RM particles and the surface of hydrated products. It not only affects the overall stability of the structure, but also hinders the creation of a gel with a larger surface area. The flake $Ca(OH)_2$ is distributed in juxtaposition within the soil with a loose inter-flake connection. Moreover, the local expansion effect of the alkali–silica gel also affects the structural strength of the soil. The above situations explain why the UCS of P.O-RMS decreases when the W_{RM} is too large (i.e., $W_{RM} > 20\%$).

At $W_{RM} = 20\%$, with the increase of W_{PO} to 12%, the content of hydration products in the soil increased, as seen from the SEM images at 28 d (Figure 17d). Among them, the coating area of CSH gel is larger, and the sheet CSH and part of $Ca(OH)_2$ are intertwined, which filled in the pores together with part of flocculent CAH to form a more compact structure.

With the increase in curing age, the P.O-RMS with $W_{RM} = 20\%$ forms a fully dense microstructure, as shown in Figure 17e, which reveals that various hydration products are combined by lap, encapsulation, and interlocking. Although there are a small number of RM particles, they are closely connected with the gel products and collectively aggregate into a stable network structure, which improves the strength of the overall gel system.

4. Conclusions

The optimal proportioning ratio of P.O-RMS can be obtained by studying the effects of various W_{RM} and W_{PO} on the P.O-RMS' mechanical properties. The variation of UCS, deformation characteristics, failure mode, and its formation mechanism of P.O-RMS are described. The conclusions of this study are drawn as follows.

- (a) With the increase of RM and W_{PO} , the w_{op} of P.O-RMS increased gradually and the ρ_{dmax} decreased gradually. As the W_{RM} increases, the water content of P.O-RMS is greater than w_{op} , resulting in an enhanced water sensitivity.
- (b) As the W_{RM} increased from 14% to 23%, there was an initial rise followed by a subsequent decline in the UCS of the specimen. At a W_{RM} of 20%, the UCS reached its peak value, at which point, the material also displayed optimal toughness and deformation-resistance characteristics.
- (c) The variation of UCS depends on the active ions of silicon and aluminum reacting chemically with Ca^{2+} –or Na^+ (or K^+) in the alkaline environment from RM to form gel products, such as C-S-H, with higher strength, or expansive products, such as Na_2SiO_3 gel, to decrease the strength.
- (d) The environmental indices of P.O-RMS under the optimal W_{RM} satisfy the requirements of China's environmental norms. The environmental impact of P.O-RMS is significantly less than that of pure RM.

In conclusion, it is very feasible to employ RM in the sustainable development of materials for roadbed filling application. It can not only solve problems related to the large accumulation of red mud, but can also effectively improve the quality of highway construction and make highway construction more environmentally friendly and safe. However, for future studies, it is recommended to evaluate the fatigue, durability, and water stability of P.O-RMS under long-term loading. In addition, long-term monitoring and evaluation of the environmental impact effects of P.O-RMS should be carried out.

Author Contributions: Conceptualization, X.L., X.Z., P.L. and Y.W.; Methodology, X.L., P.Y., S.Y. and X.Z.; Validation, X.L., P.Y., P.L. and Y.W.; Formal analysis, X.L.; Investigation, X.L., P.Y., S.Y., X.Z. and P.L.; Resources, S.Y.; Data curation, P.Y. and Y.W.; Writing—original draft, X.L.; Writing—review & editing, P.Y. and S.Y.; Supervision, S.Y.; Project administration, S.Y.; Funding acquisition, S.Y. All authors have read and agreed to the published version of the manuscript.

Funding: The authors gratefully thank the financial support of the National Natural Science Foundation of China (Nos. 51709290, Song Yin and 41972285, Xianwei Zhang), the Young Key Teachers in Colleges and Universities of Henan Province (No. 2020GGJS136, Song Yin), Key Research Projects of Higher Education Institutions in Henan Province (22A580008, Song Yin), Science Fund for Distinguished Young Scholars of Hubei Province (2020CFA103, Xianwei Zhang) and the strength improvement plan of the advantageous disciplines of Zhongyuan University of Technology (No. GG202218, Song Yin).

Institutional Review Board Statement: Not applicable.

Informed Consent Statement: Informed consent was obtained from all subjects involved in the study.

Data Availability Statement: All of the data that support the findings of the study are available from the corresponding author at reasonable request.

Conflicts of Interest: All authors disclosed no relevant relationships.

References

1. Feng, Y.; Yang, C. Analysis on physical and mechanical properties of red mud materials and stockpile stability after dilatation. *Adv. Mater. Sci. Eng.* **2018**, *2018*, 8784232. [[CrossRef](#)]
2. Mukiza, E.; Zhang, L.; Liu, X.; Zhang, N. Utilization of red mud in road base and subgrade materials: A review. *Resour. Conserv. Recycl.* **2019**, *141*, 187–199. [[CrossRef](#)]
3. Salih, W.T.; Yu, W.; Dong, X.; Hao, W. Study on stress-strain-resistivity and microscopic mechanism of red mud waste modified by desulphurization gypsum-fly ash under drying-wetting cycles. *Constr. Build. Mater.* **2020**, *249*, 118772. [[CrossRef](#)]
4. Khanna, R.; Konyukhov, Y.V.; Burmistrov, I.; Cayumil, R.; Belov, V.A.; Rogachev, S.O.; Leybo, D.V.; Mukherjee, P.S. An innovative route for valorising iron and aluminium oxide rich industrial wastes: Recovery of multiple metals. *J. Environ. Manag.* **2021**, *295*, 113035. [[CrossRef](#)]
5. Sadangi, J.K.; Das, S.P.; Tripathy, A.; Biswal, S.K. Investigation into recovery of iron values from red mud dumps. *Sep. Sci. Technol.* **2018**, *53*, 2186–2191. [[CrossRef](#)]
6. Narayanan, S.L.; Venkatesan, G.; Potheher, I.V. Equilibrium studies on removal of lead (II) ions from aqueous solution by adsorption using modified red mud. *Int. J. Environ. Sci. Technol.* **2018**, *15*, 1687–1698. [[CrossRef](#)]
7. Belviso, C.; Kharchenko, A.; Agostinelli, E.; Cavalcante, F.; Peddis, D.; Varvaro, G.; Yaacoub, N.; Mintova, S. Red mud as aluminium source for the synthesis of magnetic zeolite. *Micropor. Mesopor. Mat.* **2018**, *270*, 24–29. [[CrossRef](#)]
8. Hou, S.M.; Gao, S.; Li, Q.Y. Preparation technology and mechanism of alkali-activated red mud based cementitious materials. *J. Concrete* **2020**, *1*, 27–31.
9. Garanayak, L. Strength effect of alkali activated red mud slag cement in ambient condition. *Mater. Today Proc.* **2021**, *44*, 1437–1443. [[CrossRef](#)]
10. Yang, W.G.; Sun, Z.Y.; Li, Y.X. Analysis of road mechanical characteristics of improved red mud solidification material. *J. Transp. Technol. Econ.* **2020**, *22*, 65–68, 74. [[CrossRef](#)]
11. Sun, Z.; Wei, J.; Cheng, Y. Study on modulus Characteristics of Modified Bayer Red Mud Roadbed. *Sino-Foreign Highw.* **2018**, *38*, 54–57.
12. Ma, Q.; Duan, W.; Liu, X.; Fang, P.; Chen, R.; Wang, T.; Hao, Z. Engineering Performance Evaluation of Recycled Red Mud Stabilized Loessial Silt as a Sustainable Subgrade Material. *Materials* **2022**, *15*, 3391. [[CrossRef](#)] [[PubMed](#)]
13. Ma, S.; Sun, Z.; Wei, J.; Zhang, X.; Zhang, L. Utilization of Modified Red Mud Waste from the Bayer Process as Subgrade and Its Performance Assessment in a Large-Sale Application. *Coatings* **2022**, *12*, 471. [[CrossRef](#)]
14. *JTG 3430-2020; Test Methods of Soils for Highway Engineering*. Ministry of Transportation: Beijing, China, 2020.
15. *ASTM D1557-09; Standard Test Methods for Laboratory Compaction Characteristics of Soil Using Modified Effort*. ASTM International: West Conshohocken, PA, USA, 2009.
16. Liang, L.; Zhang, J.; Fang, P.; Suo, C. Study on Properties of Copper-Contaminated Soil Solidified by Solid Waste System Combined with Cement. *Sustainability* **2022**, *14*, 5604. [[CrossRef](#)]
17. Zhang, Z.; Xie, C.; Sang, Z.; Li, D. Optimizing the Mechanical Performance and Microstructure of Alkali-Activated Soda Residue-Slag Composite Cementing Materials by Various Curing Methods. *Sustainability* **2022**, *14*, 13661. [[CrossRef](#)]
18. Yuan, S.; Wang, R.; Zhang, H.; Li, Y.; Liu, L.; Fu, Y. Investigation of Mineral Phase Transformation Technology Followed by Magnetic Separation for Recovery of Iron Values from Red Mud. *Sustainability* **2022**, *14*, 13787. [[CrossRef](#)]

19. GB/T 15555.12-1995; Solid Waste—Glass Electrode Test—Method of Corrosivity. Ministry of Ecology and Environment: Beijing, China, 1995.
20. GB 5085.1-2019; Identification Standards for Hazardous Wastes-Identification for Corrosivity. Ministry of Transportation: Beijing, China, 2019.
21. GB 5085.3-2019; Identification Standards for Hazardous Wastes-Identification for Extraction Toxicity. Ministry of Transportation: Beijing, China, 2019.
22. GB 6566-2010; Limits of Radionuclides in Building Materials. Standardization Administration of China: Beijing, China, 2010.
23. GB 5085.7-2019; General Standard for Identification of Hazardous Waste. Ministry of Ecology and Environment: Beijing, China, 2019.
24. He, J.; Wang, X.Q.; Shi, X.K. Unconfined Compressive Strength and Microscopic Characteristics of Soft Soil Solidified with Soda Residue and Ground Granulated Blast Furnace Slag. *J. Chin. J. Appl. Basic Eng. Sci.* **2021**, *29*, 376–386. [[CrossRef](#)]
25. JTG/T F20-2015; Technical Specification for Highway Pavement Base Construction. Ministry of Transportation: Beijing, China, 2015.
26. Huang, Y.; Zhou, Z.; Bai, J.; Chen, Q. Micro-experiments on a soft ground improved by cement-mixed soils with gypsum additive. *Geotech. Eng.* **2010**, *32*, 1179–1183.
27. Cai, G.; Zhou, Y.; Pan, Z.; Li, J. Physical and mechanical performance of quicklime-activated GGBS stabilized Hong Kong marinesediment at high water content. *Geotechnics* **2022**, *43*, 327–336. [[CrossRef](#)]
28. Liu, Z.; Li, H.; Huang, M.; Jia, D.; Zhang, N. Effects of cooling method on removal of sodium from active roasting red mud based on water leaching. *Hydrometallurgy* **2017**, *167*, 92–100. [[CrossRef](#)]
29. Krivenko, P.; Kovalchuk, O.; Pasko, A.; Croymans, T.; Hult, M.; Lutter, G.; Vandevenne, N.; Schreurs, S.; Schroeyers, W. Development of alkali activated cements and concrete mixture design with high volumes of red mud. *Constr. Build. Mater.* **2017**, *151*, 819–826. [[CrossRef](#)]
30. Zhang, J.; Zhang, N.; Li, C.; Zhang, Y. Strength development mechanism of a marine binding material with red mud and seawater. *Constr. Build. Mater.* **2021**, *303*, 124428. [[CrossRef](#)]

Disclaimer/Publisher's Note: The statements, opinions and data contained in all publications are solely those of the individual author(s) and contributor(s) and not of MDPI and/or the editor(s). MDPI and/or the editor(s) disclaim responsibility for any injury to people or property resulting from any ideas, methods, instructions or products referred to in the content.